Dopant substitution and oxygen migration in the complex perovskite oxide $Ba_3CaNb_2O_9$: A computational study

Enrique Ruiz-Trejo[a,*], Roger A. De Souza[b]

[a]*Max Planck Institut für Festkörperforschung, Heisenbergstr. 1, 70569 Stuttgart, Germany*
[b]*Institut für Physikalische Chemie, RWTH Aachen, Templergraben 59, Aachen 52056, Germany*

Abstract

Atomistic simulation methods have been used to study the defect chemistry of the complex perovskite oxide $Ba_3CaNb_2O_9$. Calculations were carried out for the hexagonal (P-3$m1$) phase and the cubic (Fm-3m) phase. The hexagonal structure is predicted to be energetically more stable at room temperature. In both structures the most favourable dopant for Nb^{5+} is found to be Ca^{2+} rather than Mg^{2+}, in contrast to the generally accepted rule that size similarities govern such processes. The diffusion of oxygen vacancies in the hexagonal and cubic phases occurs within different networks of corner-sharing NbO_6 and CaO_6 octahedra. Irrespective of the arrangement of octahedra, however, migration of oxygen vacancies around NbO_6 octahedra takes place with lower activation energies than around the CaO_6 octahedra.

1. Introduction

A number of compounds based on complex perovskites with the general formula $A_3(B'B''_2)O_9$ (A cations have a charge of $2+$; B' ions, $2+$; and B'', $5+$) have recently attracted interest as high-temperature proton conductors [1] and as dielectric resonators [2]. The series $Ba_3Ca_{1+x}Nb_{2-x}O_{9-3x/2}$ in particular has been the subject of several studies on account of its high proton conductivity and chemical stability. Increasing the B'/B'' ratio in such oxides results in the formation of oxygen vacancies, which can be filled with OH^- species upon annealing samples in water vapour at high temperatures.

Even though the OH^- concentration may be small, the ionic conductivity can be dominated by proton transport [3]. Oxygen vacancies in simple ABO_3 perovskites are known to be highly mobile, but in complex perovskites, such as $Ba_3Ca_{1+x}Nb_{2-x}O_{9-3x/2}$, this transport process has received scant attention. In this study we used atomistic simulation methods to examine the energetics of oxygen migration and the energetics of the related issues of oxide formation and dopant substitution in this complex perovskite, in order to aid the interpretation of, and give direction to, experimental research.

The simulation methods we used have been applied successfully to the study of the crystallographic structures and the mechanisms of defect generation and migration in various ionic solids, such as $LaYO_3$ [4], $LaInO_3$ [5], $LaGaO_3$ [6,7], $LaMnO_3$ [8,9], $LnAlO_3$ [10] and $LiNbO_3$ [11]. We note that defect processes involving protons are more suited to investigation with quantum mechanical methods [12,13].

*Corresponding author. Present address: Facultad de Química UNAM, Departamento de Física y Química Teórica, Cd. Universitaria, 04510 México, D.F. Fax: +52 55 56 22 35 21.

E-mail address: enrique.ruiz_trejo@servidor.unam.mx (E. Ruiz-Trejo).

Table 1

Interaction	A (eV)	ρ (Å)	C (eVÅ^6)	Ref.
(a) *Short-range interatomic potentials*				
Ba^{2+}–O^{2-}	931.7	0.3949	0	[15]
Ca^{2+}–O^{2-}	1228.9	0.3372	0	[15]
Nb^{5+}–O^{2-}	1796.3	0.34598	0	[11]
O^{2-}–O^{2-}	22764.3	0.149	27.879	[11,15]

Ion		Y (e)		K (eVÅ^{-2})
(b) *Shell model parameters*				
Ba^{2+}		1.46		14.78
Ca^{2+}		1.26		34
Nb^{5+}		−4.496		1358.58
O^{2-}		−2.811		103.07

2. Methods

The details of the methodology of the atomistic simulation techniques are described extensively elsewhere [14] and here we will only present a short summary. The basis of the computer simulation technique is the specification of a potential model, i.e., the description in mathematical terms of the system energy as a function of particle co-ordinates. The Born model representation is commonly used for these oxides, for which the energy is partitioned into long-range Coulombic interactions and short-range pair potentials:

$$V_{ij}(r) = \kappa \frac{q_i q_j}{r_{ij}} + A_{ij} \exp\left[\frac{-r_{ij}}{\rho_{ij}}\right] - \frac{C_{ij}}{r_{ij}^6}, \qquad (1)$$

where κ is a constant in suitable units, q_i and q_j are the integral charge of ions i and j, respectively, and r_{ij} is the inter-ionic distance; A_{ij}, ρ_{ij} and C_{ij} are empirical parameters assigned to each ion–ion interaction, with the exception of cation–cation interactions, which were treated as purely Coulombic. The model we used was essentially ionic; no covalent term was explicitly included in our calculation. The interatomic potentials used in these systems are indicated in Table 1 and were originally derived for studies of alkaline earth oxides [15] and of LiNbO$_3$ [11]. No further refinement was carried out.

In some cases fractional occupancies were required for certain crystallographic sites. This was implemented through a mean-field approach, that is, the site is assumed to contain a hybrid ion, e.g., Ca$_z$Nb$_{1-z}$, for which the potential energy V_{ij} is proportional to the site fraction occupancy:

$$V_{(Ca_zNb_{1-z})-O} = z V_{Ca-O} + (1-z) V_{Nb-O}. \qquad (2)$$

As charged defects will polarise other ions in the lattice, it is necessary to incorporate ionic polarisability into the model. Polarisation is treated by means of the shell model [16] which regards each ion in terms of a core connected via a harmonic spring to a mass-less shell. Displacement of the shell relative to the core gives a good description of electronic polarisation of ions.

The calculations in perfect and defective lattices are based on well-established energy minimisation procedures. In these, all ions are relaxed to a minimum energy configuration using a Newton–Raphson procedure for which both the first and second derivatives of the energy with respect to strain must be calculated. A key feature of these calculations is the treatment of lattice relaxations around a point defect or migrating ion using the Mott–Littleton methodology. This approach involves the partition of the crystal lattice around a point defect in a spherical inner region where ions are relaxed explicitly. In contrast, the remainder of the crystal is treated by more approximate quasi-continuum methods [11,15].

3. Results

3.1. Perfect lattice simulation

3.1.1. Cubic structure

The cubic phase proposed for Ba$_3$CaNb$_2$O$_9$ is based on the *Fm*-3*m* space group [17]. It is depicted in Fig. 1 as a network of two different types of corner-sharing octahedra: those containing only Nb and those containing on average Ca$_{2/3}$Nb$_{1/3}$. Each Ca$_{2/3}$Nb$_{1/3}$O$_6$ octahedron shares corners with six NbO$_6$ octahedra and vice versa. In order to model the perfect lattice we used a mean-field approach for (4b) Ca$_{2/3}$Nb$_{1/3}$ positions. The calculated properties are listed in Table 2. Without adjustment of the empirical parameters, the lattice constant is reproduced to within 2%, and the static dielectric permittivity is close to the experimental value. We emphasise that, even though the cell parameters are not exactly reproduced, we do have the
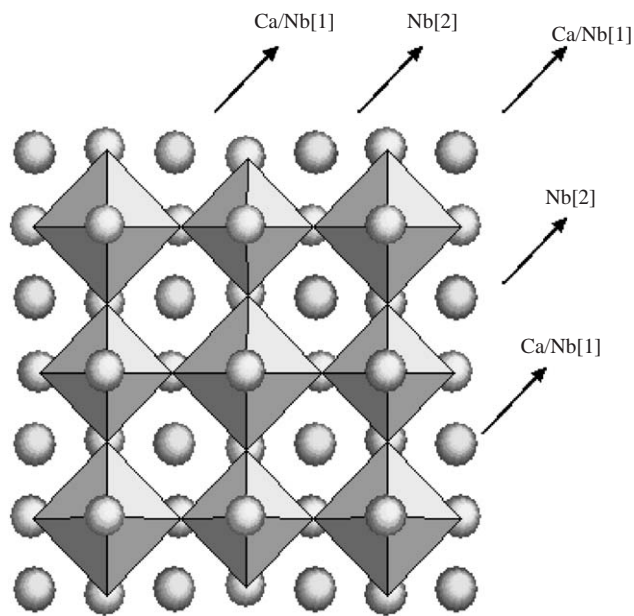
Fig. 1. The cubic perovskite $Ba_3CaNb_{0.5}Nb_{1.5}O_9$ can be depicted as a network of interconnected large and small octahedra. The small octahedra contain Nb(2) in the center and oxygen in the corners while the large octahedra contain an averaged $Ca_{0.67}Nb(1)_{0.33}$ in the center and O in the corners. Oxygen ions are depicted at the corners of the octahedra while the other spheres represent barium ions. The arrows indicate the 1:1 order. Space group Fm-$3m$. Atomic positions: (8c) Ba $\frac{1}{4}, \frac{1}{4}, \frac{1}{4}$; (4$b$) Ca/Nb(1) $0\,0\frac{1}{2}$; (4a) Nb(2) $0\,0\,0$, (24e) O 0.2359, 0, 0.
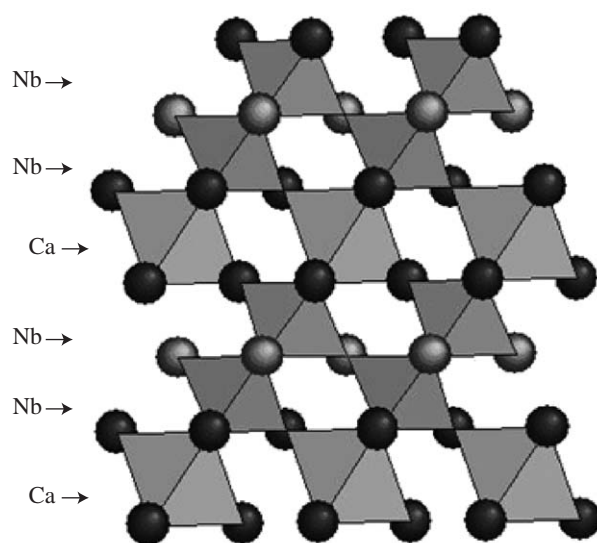

Fig. 2. The hexagonal perovskite $Ba_3CaNb_{0.5}Nb_{1.5}O_9$ depicted as a network of octahedra. The large octahedra are CaO_6 and the small octahedra are $NbO(1)_3O(2)_3$. A long-range order oxygen migration necessarily involves the CaO_6 octahedra. No Ba atoms are shown. The arrows indicate the 2:1 order. Space group P-$3m$1, Atomic positions Ba(1) (1a) $0\,0\ \ 0$; Ba(2) (2d) $\frac{1}{3}, \frac{2}{3}, 0.6487$; Ca (1$b$) $0, 0, \frac{1}{2}$; Nb (2d) $\frac{1}{3}, \frac{1}{3}, 0.1634$; O(1) (3$e$) $\frac{1}{2}, 0, 0$; O(2) (6i) 0.1855, 0.8145, 0.3086.

Table 2
Properties of cubic $Ba_3CaNb_2O_9$

Property	Calculated	Experimental
Cohesive energy per unit formula (eV)	−145.59	—
Cell parameter (Å)	8.5193	8.3630 [18]
O atomic position	0.2359	0.26139(11) [19][a]
Bulk modulus (GPa)	157	100±8 [20]
Static dielectric permittivity	24	20 [21]
High-frequency dielectric permittivity	1.9	—

[a]For $Ba_3Ca_{1.10}Nb_{1.90}O_{9-\delta}$.

Table 3
Properties of hexagonal $Ba_3CaNb_2O_9$

Property	Calculated	Experimental
Cohesive energy per unit formula (eV)	−152.28	—
Cell parameters a (Å)	6.0722	5.92 [17]
c (Å)	7.4925	7.25 [17]
Bulk modulus (GPa)	132	—
Static dielectric constant	12	—
High-frequency dielectric constant	1.9	—

benefit that the potentials used are valid at a variety of separations.

3.1.2. Hexagonal structure

The hexagonal structure proposed for $Ba_3CaNb_2O_9$ is based on the P-$3m$1 space group [22]. In contrast to the cubic phase, this structure has unique crystallographic sites for the Ca and Nb ions (in addition to two crystallographic positions for the Ba ions and two for the O ions), as indicated in Fig. 2. The arrangement of the (corner-sharing) CaO_6 and NbO_6 octahedra is such that there is a NbO_6–NbO_6–CaO_6 stacking sequence along [100] (which corresponds to [111] in the cubic cell).

On account of this stacking, the hexagonal structure is commonly referred to as having a 2:1 order.

Since there are no crystallographic sites that are occupied by more than one type of ion, we do not need to use a mean-field approach in order to model the perfect structure. A comparison of some calculated physical properties and the available experimental data is given in Table 3. It is noted that, even though hexagonal cell parameters are just under 3% greater than the experimental values, the calculated c/a ratio of 1.234 is nevertheless in close agreement with the experimental value of 1.225.
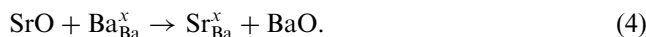
3.2. Cation substitution

$Ba_3CaNb_2O_9$ and similar compounds are often doped with alkaline earth oxides, in some cases, in order to achieve high proton conductivity, and in others, to tune the dielectric properties. For this reason we examined,

for both structures, the substitution of alkaline earths for the constituent cations.

Regardless of the cation site, there are principally two types of substitution reaction: substitution for Nb, with the formation of oxygen vacancies,

$$3O_O^x + 2CaO + 2Nb_{Nb}^x \rightarrow 2Ca_{Nb}''' + 3V_O^{\bullet\bullet} + Nb_2O_5 \quad (3)$$
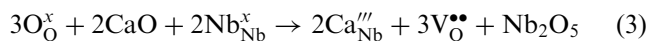
and alkaline earth oxide substitution, e.g.,

$$SrO + Ba_{Ba}^x \rightarrow Sr_{Ba}^x + BaO. \quad (4)$$

3.2.1. Cubic structure

The mean-field approach used to model the perfect lattice of the cubic structure is not appropriate for examining substitution reactions, because the substitution of a hybrid cation is physically unrealistic. In other words, with regard to the $4b$ $Ca_{2/3}Nb_{1/3}$ site, one has to consider the substitution of an alkaline earth, either for a Nb^{5+} ion sitting on this site or for a Ca^{2+} ion sitting on this site. Consequently, we generated a supercell, comprising $3 \times 1 \times 1$ cubic unit cells, and randomly distributed 8 Ca ions and 4 Nb(1) ions over the twelve $4b$ sites. The energy of a cation substituting for each of these atomic sites was computed. We then averaged the energy of the various cation substitutions, and by combination of the appropriate energetic terms, we obtained an estimation of the energy of cation substitution.

The energies obtained for the substitution reactions are plotted in Fig. 3 as a function of the dopant cation radius in that particular coordination. Two important points emerge, regarding the differing behaviour of the two Nb sites. First, we see that the energies for alkaline earth substitution for Nb(2) are large in comparison with those for Nb(1). In the case of $Ba_3Ca_{1+x}Nb_{2-x}O_{9-3x/2}$, for example, the calculations clearly show that the excess Ca is accommodated on the

Nb(1) site: $E_{sub}^{Nb[1]} = 4.0\,eV$ per mole of CaO, $E_{sub}^{Nb[2]} = 9.3\,eV$ per mole of CaO. Furthermore, we find that the most favourable dopant for Nb(2) is Mg, as expected from their similar radii ($r(Nb^{5+}) = 0.64\,\text{Å}$, $r(Mg^{2+}) = 0.72\,\text{Å}$), whereas in the case of Nb(1) more favourable reaction energies are found for Ca^{2+} ($r = 1.00\,\text{Å}$) or even Sr^{2+} ($r = 1.18\,\text{Å}$).

We emphasise that Eqs. (3) and (4) describe substitution reactions and not doping reactions. The former corresponds to the addition of a dopant oxide causing the displacement of an oxide component; the latter require the simultaneous addition of dopant and the removal of that oxide component. This point is emphasised for the reason that the reaction energies for Ca displacing Ba are lower than for Ca displacing Nb; this does not mean that the calculations predict Ca doping to be energetically unfeasible.

3.2.2. Hexagonal structure

Fig. 4 displays the energy of the solution of alkaline earth oxides into the different cationic sites. As in the case of the cubic phase, the substitution energy of Ca^{2+} for Nb^{5+} is more favourable than that of Mg^{2+}, even though in terms of size matching Mg^{2+} would be considered to be a better substitute for Nb^{5+}. It can also be seen in Fig. 4 that the solution energies of CaO and SrO in the Ca (1b) sites are very similar and that the latter is even slightly more favourable. Note that according to our calculations, Ba could also be replaced by Sr without a large expenditure of energy.

3.3. Oxygen migration

Computational studies of a host of simple perovskite oxides indicate that oxygen migration takes place by the exchange of oxygen vacancies with oxygen ions along the edges of the BO_6 octahedra [4–6,9]. Consequently,
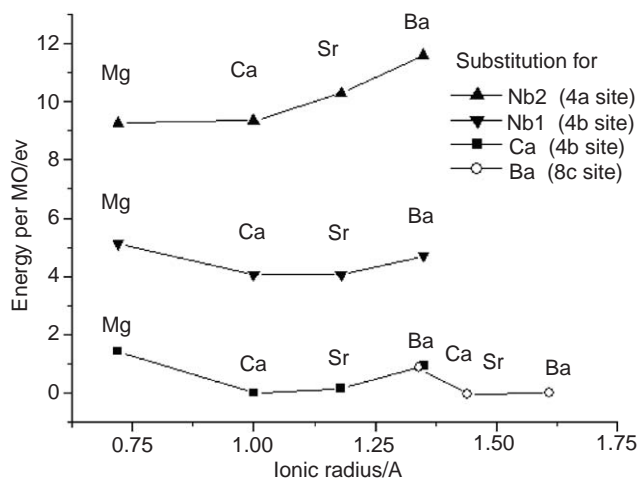

Fig. 3. Substitution energies of alkaline earth oxides into cubic $Ba_3CaNb_2O_9$. Ionic radii from Shannon [33].
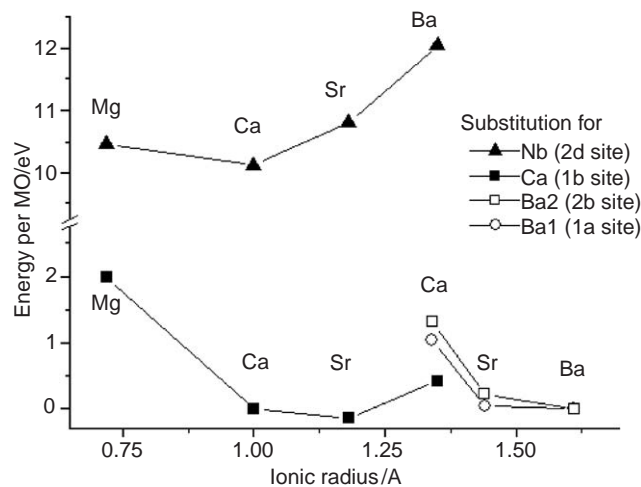

Fig. 4. Substitution energies of alkaline earth oxides into hexagonal $Ba_3CaNb_2O_9$. Ionic radii from Shannon [33].

we examined this migration mechanism for each of the various BO_6 octahedra in the complex perovskite $Ba_3CaNb_2O_9$. The procedure for obtaining the activation energies for oxygen migration in cubic and hexagonal $Ba_3CaNb_2O_9$ was, therefore, essentially that employed previously [4–6,9]: an oxygen ion is fixed at various positions between its initial site and a neighbouring vacant site, and the defect energy at each point is calculated. By probing the energy surface in this manner one can determine the migration path and the saddle point configuration, and consequently, the migration energy.

3.3.1. Cubic structure

Recalling the description of the cubic structure in terms of two types of octahedra, it is clear that there are essentially three different possible jumps: along the edge of a $Nb(2)O_6$ octahedron, along the edge of a $Nb(1)O_6$ octahedron, and along the edge of a CaO_6 octahedron. While the calculations for the $Nb(2)O_6$ octahedron do not present a problem, simply modelling the $4b$ site using hybrid cations would be inappropriate, since the specific pair interactions would be lost. Our method to examine oxygen vacancy migration around the cations occupying the $4b$ site consisted of combining mean-field and supercell approaches. First of all we generated a $3 \times 1 \times 1$ supercell containing hybrid Ca/Nb cations. In order to examine oxygen vacancy migration, for example, along a Nb(1) octahedron, we substituted the hybrid Ca/Nb(1) ion at the centre of the supercell with an Nb^{5+} and adjusted the Ca/Nb ratio of the remaining hybrid sites to give an electrically neutral supercell (see Fig. 5). This enables us to model accurately the $Nb(1)O_6$ octahedron and its near surroundings, while providing a good approximate description of the rest of the crystal. Analogous calculations were also carried out for the case of a Ca^{2+} in the central octahedron.

The calculated migration energies are listed in Table 4. It is seen that the energies of migration around NbO_6 octahedra are almost half that for a CaO_6 octahedron. As reported in previous works [4–6,9], the migration paths did not follow straight lines along the edges of the octahedra, but rather curved paths, as sketched in Fig. 5. The curvature was found to be less pronounced in case of the NbO_6 octahedra compared to that of the CaO_6 octahedron.

3.3.2. Hexagonal structure

As indicated in Fig. 2, the hexagonal structure is based on octahedra containing only Ca or only Nb, and also possesses two different crystallographic sites for oxygen ions. Consequently, one finds that there are 5 different possible exchanges for oxygen ions and vacancies. The migration energies calculated for these jumps are listed in Table 5. The trend observed
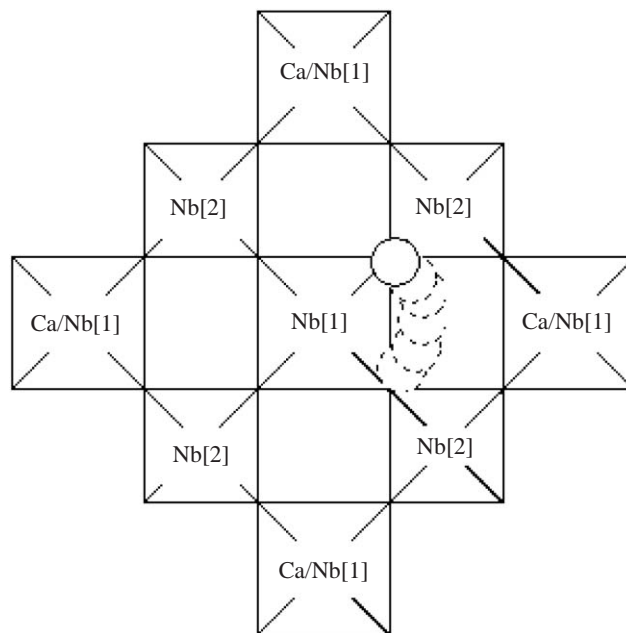

Fig. 5. Configuration used to examine oxygen migration in cubic $Ba_3CaNb_2O_9$. A $Nb(1)O_6$ octahedron is shown in the center. The ratio of the rest $Ca/Nb(1)O_6$ octahedra are modified as to give an overall neutral cell.

Table 4
Migration energies for oxygen vacancy jumps along the edge of various octahedra in cubic $Ba_3CaNb_2O_9$

Octahedron	d_{O-O}/Å	ΔE_m/eV
$Nb(2)O_6$	2.83	0.73
$Nb(1)O_6$	2.86	1.05
CaO_6	3.35	2.03

Table 5
Migration energies for oxygen vacancy jumps along the edge of various octahedra in hexagonal $Ba_3CaNb_2O_9$

Octahedron	Oxygen sites	d_{O-O}/Å	ΔE_m/eV
$NbO(1)_3O(2)_3$	O(2)–O(2)	2.69	0.48
$NbO(1)_3O(2)_3$	O(2)–O(1)	2.85	0.93
$NbO(1)_3O(2)_3$	O(1)–O(1)	3.04	1.57
$CaO(2)_6$	O(2)–O(2)	3.38	2.25
$CaO(2)_6$	O(2)–O(2)	3.47	2.77

in the cubic structure is repeated here: jumps around the Nb octahedra are of lower energy than jumps around the CaO_6 octahedron. Furthermore, there is a correlation between jump distance and activation energy.

4. Discussion

4.1. Structure

Despite several studies of this material, there are still some uncertainties concerning the exact crystallographic symmetry adopted by $Ba_3Ca_{1+x}Nb_{2-x}O_{9-3x/2}$ compounds [18,21,23–26]. In the literature both cubic [21] and hexagonal [24] structures have been proposed for the room temperature structure of $Ba_3CaNb_2O_9$. Our calculated lattice energies (see Tables 2 and 3) indicate that the hexagonal modification is the energetically more stable structure at room temperature. From an experimental point of view, however, one can imagine that the additional cation ordering required to form the hexagonal structure necessitates high temperatures and long anneal times, cation transport in perovskite oxides being characterised by very high migration energies [7,8]. Insufficient thermal treatment may therefore explain why the cubic form is often observed at room temperature. Indeed, in an experimental study of a similar complex oxide $Ba_3MgNb_2O_9$, a cubic structure was obtained at room temperature after annealing at $T_s = 1000\,°C$, whereas an anneal at a higher temperature, $T_s = 1300\,°C$, yielded the 2:1 hexagonal structure [27].

We briefly comment here on the structures of the $Ba_3Ca_{1+x}Nb_{2-x}O_{9-3x/2}$ materials, which are reported to be hexagonal [17] ($x = 0$, $T_s = 1400\,°C$, $t_s = 4\,h$), cubic ($x = 0.18$, $T_s = 1400\,°C$, $t_s = 2\,h$) [26], ($T_s = 1250\,°C$, $t_s = 3\,h$) [21], or even a mixture of both and an extra disordered cubic phase [24]. Du and Nowick observed that increasing x induces a gradual structural transformation from hexagonal to cubic symmetry [24]. In contrast, other researchers found that $Ba_3Ca_{1+x}Nb_{2-x}O_{9-3x/2}$ ($x = 0–0.18$) samples sintered at $1200\,°C$ for $4\,h$ all adopted a cubic structure [18] whereby the annealing conditions probably inhibited the formation of the hexagonal phase, at least for the parent compound. A structural transformation to the cubic form is expected as x increases, since Ca substitution will disrupt the 2:1 order of the hexagonal structure. It is unclear, however, whether the transition occurs over a range of x values, such that $Ba_3Ca_{1.18}Nb_{1.82}O_{9-\delta}$, for instance, is a mixture of cubic and hexagonal phases [23], or whether it is abrupt, such that $Ba_3Ca_{1.18}Nb_{1.82}O_{9-\delta}$ is cubic [18,26]. Elucidation is made more complex by having the sintering temperature as a variable, with higher temperatures promoting the hexagonal 2:1 ordering and lower temperatures the cubic structure, as described above for $Ba_3MgNb_2O_9$ [27] and also for $Sr_{0.2}Ba_{0.8}(SrTa_2)O_9$ [29].

Further support for our modelling work can be found by comparing the calculated static dielectric constants with experimental results. As can be seen in Table 2, ε_s for the cubic structure is in reasonable agreement with the single available result. According to our calculations, the dielectric constant in the 1:1 cubic structure is reduced to half the value of that in the 2:1 hexagonal structure. Such a dramatic reduction in the value of the dielectric constant upon ordering has been observed experimentally in other complex perovskites, for example, in $Ca_3(CaNb_2)O_9$ [28] and $Sr_{3-x}Ba_x(SrTa_2)O_9$ [29]. For the latter system, the 1:1 ordered $Sr_3(SrTa_2)O_9$ has an ε_s of ca. 33, which drops by almost half to 18 for the 2:1 ordered compound $Sr_{0.3}Ba_{2.7}(Sr_1Ta_2)O_9$ [29]. Takahashi et al. [29] conclude the behaviour is due to the 2:1 ordering rather than to the Ba substitution for Sr.

4.2. Dopant substitution

Alkaline earth dopants were found to show a marked preference for substituting for Nb(1) rather than for Nb(2) in the cubic structure. This is a surprising result because the immediate environments of the two Nb ions are only marginally different (the calculated Nb–O distances are 2.02 and 2.00 Å, respectively).

We propose that this behaviour is due to the relative ease of deforming NbO_6 octahedra in comparison with CaO_6 octahedra. Comparing 48 Ca–O distances for octahedra in various inorganic structures [30,31] we calculate an average distance of 2.39 ± 0.12 Å, which indicates that the CaO_6 octahedra are rather large and relatively incompressible. Indeed, in the structurally similar compound, $Sr_3CaRu_2O_9$, even though the two crystallographically distinct Ca are under compression, the bond lengths are almost identical, 2.231 ± 0.012 and 2.215 ± 0.007 [31]. In contrast, many niobium oxide compounds are based on NbO_6 octahedra that display a variety of Nb–O distances (from 2.301 to 1.947 Å) and that are distorted to varying extents [32,33] If one now considers the radii of the dopant alkaline earth cations, one notices that they are all larger than Nb^{5+} (Shannon's value of 0.64 Å is remarkably close to values obtained for this structure, if one assumes Shannon's value of 1.40 Å for the oxygen ion radius). Hence, substitution for Nb^{5+} compresses the surrounding lattice. In the case of substitution for Nb(1) the adjacent octahedra are all $Nb(2)O_6$, which deform with a relatively small expenditure of energy upon the introduction of a large, alkaline earth cation. The contraction of the surrounding lattice is also required when alkaline earth cations substitute for Nb(2), but in this case the deformation is energetically expensive, because, on average, two-thirds of the adjacent octahedra are incompressible CaO_6 octahedra. Experimental evidence to support our proposal comes from a neutron diffraction study of $Ba_3Ca_{1+x}Nb_{2-x}O_{9-3x/2}$ by Oikawa et al. [19] They observed a decrease in the volume of the $Nb(2)O_6$ octahedra with increasing Ca doping, but discounted this finding in favour of a far more complicated (rhombohedral) structure.

With regard to the hexagonal structure we note that such issues are irrelevant, since there is only one crystallographic site for Nb; we reiterate that the introduction of extra Ca in $Ba_3Ca_{1+x}Nb_{2-x}O_{9-3x/2}$ disrupts the 2:1 order, the higher the Ca excess, the more disorder created.

It is generally accepted that the solution energies for a range of isovalent dopant cations display a minimum when the radius of the dopant cation is close or equal to that of the lattice ion it is displacing [10]. Consequently, one would expect that, of Mg^{2+}, Ca^{2+}, Sr^{2+} and Ba^{2+}, magnesium would be the most favourable substituent for Nb^{5+}. Considering together the results obtained for the cubic structure (two Nb sites) and the hexagonal structure (one Nb site), we find that, in contrast to this rule, Ca^{2+} and Sr^{2+} are more favourable dopants in two out of three cases, $Nb(1)_{cub}$ and Nb_{hex}. As before, the difference may be related to the cations occupying the surrounding octahedra. $Nb(1)_{cub}O_6$ is linked to six NbO_6 octahedra, $Nb_{hex}O_6$ to four NbO_6 octahedra and two CaO_6 octahedra, whereas $Nb(2)_{cub}O_6$, for which Mg^{2+} is the preferred substituent, is surrounded by more CaO_6 octahedra (4/6) than NbO_6 octahedra (2/6). That much larger dopant cations are preferred suggests that Nb^{5+} and O^{2-} would like to be much closer together than the perfect structure allows.

Another interesting result of our calculations is that Sr^{2+} can favourably substitute for Ca^{2+} in the hexagonal structure or Ba^{2+} in both the cubic and the hexagonal structures. From the defect chemistry point of view, these seem to be rather irrelevant substitutions. As some experimental results in $Sr_{1-x}Ba_x(Sr_{1/3}Ti_{2/3})O_3$ indicate, however, such substitution can induce a cubic 1:1 ($x = 0$) or a hexagonal 2:1 ($x = 1$) structure [29]. This may allow the tuning of dielectric properties.

4.3. Oxygen migration

From the data given in Tables 4 and 5 we can conclude that oxygen vacancy jumps around NbO_6 octahedra have lower activation energies than jumps around CaO_6 octahedra, regardless of the exact crystal symmetry, and hence that the difference in behaviour arises from the different sizes and charges of the octahedral cations.

The saddle point configurations identified in our calculations consist of the oxygen ions passing through the aperture formed by two Ba cations and the B site cation (Ca or Nb), as expected from previous work on oxygen migration in perovskites [9,10]. Kilner and Brook [10] noted that the radius of a sphere that can just pass through this aperture without disturbing the surrounding lattice, the critical radius, is smaller than that of an oxygen ion. These cations thus constitute a steric hindrance to oxygen migration.
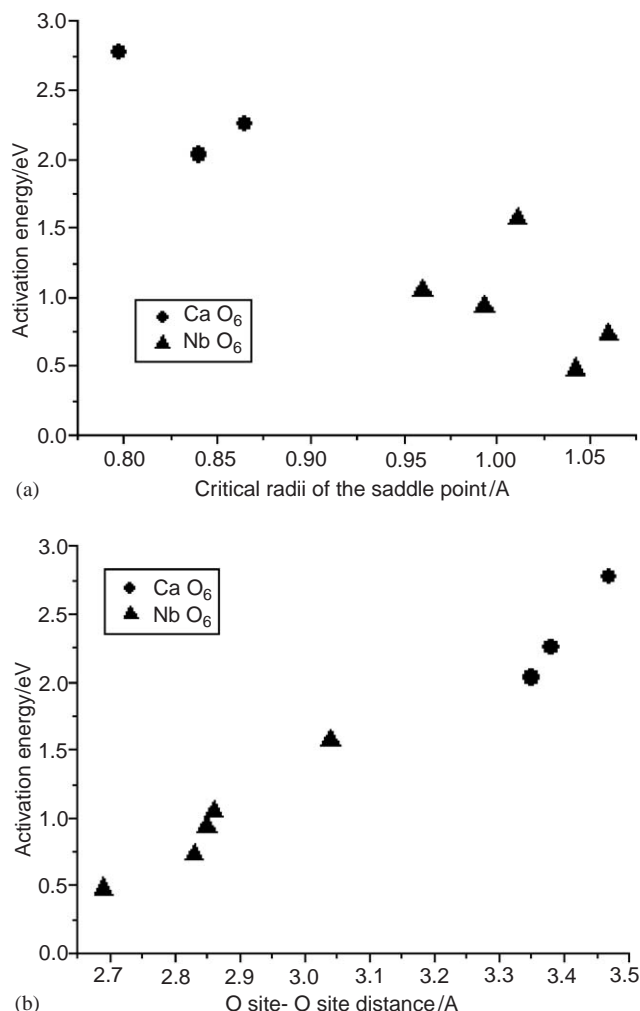

Fig. 6. Activation energy for oxygen transport (a) as a function of saddle point radii and (b) as a function of the O site–O site distance for the two types of octahedra.

We estimated the critical radii of the various saddle points, using the cations' positions in the unit cells and their Shannon radii $\{r(Ba^{2+}) = 1.61\,\text{Å}$; $r(Nb^{5+}) = 0.64\,\text{Å}$; $r(Ca^{2+}) = 1.00\,\text{Å}\}$ [33]. As shown in Fig. 6a, there is a clear difference between the CaO_6 and NbO_6 octahedra, or rather between the Ca–Ba–Ba and Nb–Ba–Ba apertures. This difference is consistent with the size of the cations playing a role in determining ΔE_m, but there are also trends within each octahedron type, which suggests that r_{crit} is not the only important parameter. A more complete description will require us to consider, in addition, the different Coulomb contributions for an O^{2-} migrating towards Nb^{5+} or Ca^{2+} and also the deformability of the surrounding octahedra (cf. dopant substitution discussed in the previous section). Lastly, we show in Fig. 6b that there is a good correlation between ΔE_m and the jump distance of the oxygen ion. The reason behind this is unclear, but as d_{O-O} is a measure of the size of the octahedron,

it may reflect both steric and coulombic contributions to ΔE_m.

Let us now consider oxygen diffusion in the system $Ba_3Ca_{1+x}Nb_{2-x}O_{9-3x/2}$. The substitution of Ca for Nb generates oxygen vacancies, which are, of course, necessary for oxygen diffusion, but at the same time leads to an increase in the number of CaO_6 octahedra, which make the migration of oxygen vacancies more difficult. Furthermore, it also drives the structural transition from hexagonal to cubic symmetry. For low values of x, such that the hexagonal structure is still stable, one can say that oxygen diffusion will be characterised by an activation energy of greater than 2 eV, since, for three-dimensional, long-range transport to occur, the oxygen vacancies must inevitably migrate at some point along a CaO_6 octahedra (recall Fig. 2). At some value of x the cubic structure will be the more stable form, and the situation becomes more complicated because of the huge variety of possible oxygen vacancy jumps within the network of CaO_6 and NbO_6 octahedra. We analysed this problem with the percolation theory: we consider all NbO_6 jump possibilities as *connected* paths, on account of their low activation energies, and all CaO_6 octahedra jumps as *unconnected* paths, on account of their higher activation energies. Each time a migrating oxygen vacancy in an $Nb(2)O_6$ octahedron moves to a different octahedron, it has six possible destinations in $Ba_3Ca_{1+x}Nb_{2-x}O_{9-3x/2}$ with $x = 0 : 2$ are *connected* $Nb(1)O_6$ and four are *unconnected* CaO_6. These six possibilities can be represented by a simple cubic lattice. The critical fraction of $Nb(1)O_6$ octahedra required to maintain a continuous *connected* path from one side of a macroscopic sample to the other, the bond percolation threshold, is 0.249 [34] which corresponds to a composition $Ba_3Ca_{1.127}Nb_{1.873}O_{8.810}$. Going below this critical fraction, i.e., increasing the amount of Ca excess, will cause the oxygen diffusivity to drop considerably, despite the increasing concentration of oxygen vacancies, and the associated activation energy to rise from ca. 1 eV to greater than 2 eV.

Kreuer and co-workers have shown for simple ABO_3 perovskites that proton migration is governed by the vibrational dynamics of the oxygen ions [13], which is determined by the potential wells in which the O^{2-} ions reside, and the Coulomb interaction between the proton and the B cation [12]. In the case of $Ba_3Ca_{1+x}Nb_{2-x}O_{9-3x/2}$ one could say, therefore, that the further substitution of Nb^{5+} with Ca^{2+} beyond the percolation threshold will cause a reduction in the repulsive Coulomb term that combined with the higher proton concentration (which is proportional to the dopant concentration), may compensate for the hardening of the oxygen-ion vibrations, up to a certain level. Interestingly, maximum proton conductivity in $Ba_3Ca_{1+x}Nb_{2-x}O_{9-3x/2}$ was observed for $x = 0.18$,

which is equivalent to a site fraction of Nb(1) ions in the 4b sites of 0.213. This value is *below*, but still close to, the percolation threshold for oxygen vacancy migration of 0.249.

In making such comparisons one must also consider that the experimental conductivity was measured with impedance spectroscopy, and hence, does not correspond to long-range transport, but only to hops that take place within half an a.c. cycle. Hence, one could be below the percolation threshold, but still have regions that are separated from one another, within which there are *connected* paths of NbO_6 octahedra. This would explain why the available experimental data on oxygen transport in $Ba_3Ca_{1.18}Nb_{1.82}O_{9-3x/2}$ give activation energies of 0.82–0.92 eV [35] and 0.7 eV [36], which can only refer to the migration of oxygen vacancies around NbO_6 octahedra. In this regard it would be of great interest to determine the d.c. conductivity data in dry samples or to measure the diffusion of isotopically labelled oxygen. Finally, we note that the possibility of having mixed phase samples complicates the analysis of experimental information.

5. Conclusions

The structures of cubic and hexagonal $Ba_3CaNb_2O_9$ were modelled by means of atomistic simulation. The calculated properties present a reasonable agreement with the experimental results available. Further support for our modelling work was found by comparing the static dielectric constant with experimental results for similar systems.

Against the generally accepted rule that size similarities should facilitate doping, we found that the substitution of Ca^{2+} for Nb^{5+} is more favourable than the substitution of Mg^{2+} for Nb^{5+} in $Ba_3CaNb_2O_9$. The introduction of a large cation such as Ca^{2+} induces the contraction of the surrounding octahedra. We suggest that the ease of deforming the surrounding NbO_6 octahedra, as opposed to the CaO_6 octahedra, is responsible for this effect. In cubic $Ba_3CaNb_2O_9$ this leads to a clear distinction between the two Nb sites. The contraction of the surrounding NbO_6 with Ca doping has indeed been reported in the literature.

There are two distinct paths for oxygen migration: transport along CaO_6 octahedra and transport along NbO_6 octahedra. The former process is hindered by the high activation energy of 2 eV while the latter is relatively easy, with an activation energy around 1 eV. The size of the saddle point aperture and the cation radii play a role in determining ΔE_m, but we also found that the activation energy decreases clearly with the migrating distance; however, further work should be carried out in order to explain this trend.

In the cubic structure oxygen migration will take place preferentially through hopping along NbO_6 octahedra. In a purely cubic $Ba_3Ca_{1+x}Nb_{2-x}O_{9-3x/2}$ oxygen migration can be facilitated by the existence of a percolation path of NbO_6 octahedra. After a composition of $Ba_3Ca_{1.1268}Nb_{1.8732}O_{9-\delta}$ any extra amount of Ca will result in the increase the activation energy as oxygen must also now migrate along CaO_6. The reported values of 0.7–0.92 eV seem to indicate that the migration of oxygen ion takes place around the NbO_6 octahedra only.

Interestingly, the percolation value of $Ba_3Ca_{1.1268}Nb_{1.8732}O_{9-\delta}$ and the composition $Ba_3Ca_{1.18}Nb_{1.82}O_{9-3x/2}$ reported to have the maximum proton conduction are very close to each other. Proton conduction might be as well affected by this percolation value since the vibrational amplitudes of two oxygen atoms is of paramount importance for the transport of protons and these are affected by the *B* cation.

In the hexagonal structure, transport along NbO_6 octahedra has an activation energy lower than 1 eV but transport along CaO_6 octahedra is higher than 2 eV. However, due to structural reasons oxygen migration involves the movement along CaO_6 octahedra, making oxygen ion migration more difficult. In a $Ba_3Ca_{1+x}Nb_{2-x}O_{9-\delta}$ system, the doping breaks the 2:1 order and may lead to a cubic structure.

Acknowledgments

References

[1] A.S. Nowick, Y. Du, K.C. Liang, Solid State Ionics 125 (1999) 303–311.

[2] T.S. Rao, V.R.K. Murthy, B. Viswanathan, Ferroelectrics 102 (1990) 155–160.

[3] K.D. Kreuer, Chem. Mater. 8 (1996) 610–641.

[4] E. Ruiz-Trejo, M.S. Islam, J.A. Kilner, Solid State Ionics 123 (1999) 121–129.

[5] E. Ruiz-Trejo, G. Tavizón, A. Arroyo-Landeros, J. Phys. Chem. Solids 64 (2003) 515–521.

[6] M.S. Khan, M.S. Islam, D.R. Bates, J. Phys. Chem. B 102 (1998) 3099–3104.

[7] R.A. De Souza, J. Maier, Phys. Chem. Chem. Phys. 5 (4) (2003) 740–748.

[8] R.A. De Souza, M.S. Islam, E. Ivers-Tiffée, J. Mater. Chem. 9 (1999) 1621–1627.

[9] M. Cherry, M.S. Islam, C.R.A. Catlow, J. Solid State Chem. 118 (1995) 125–132.

[10] J.A. Kilner, R.J. Brook, Solid State Ionics 6 (1982) 237–252.

[11] H. Donnerberg, S.M. Tomlinson, C.R.A. Catlow, O.F. Schirmer, Phys. Rev. B 40 (1989) 11909–11916.

[12] W. Münch, K.-D. Kreuer, G. Seifert, J. Maier, Solid State Ionics 125 (1999) 39–45.

[13] W. Münch, G. Seifert, K.D. Kreuer, J. Maier, Solid State Ionics 97 (1997) 39–44.

[14] C.R.A. Catlow, in: A.D. Cheetham, P. Day (Eds.), Solid State Chemistry—Techniques, Clarendon Press, Oxford, 1987, p. 231.

[15] G.V. Lewis, C.R.A. Catlow, J. Phys.Chem. Solid State Phys. 18 (1985) 1149–1161.

[16] B.G. Dick, A.W. Overhauser, Phys. Rev. 112 (1958) 90–103.

[17] F.S. Galasso, Perovskites and High Tc Superconductors, Gordon and Breach Science Publishers, Amsterdam, 1990.

[18] E. Ruiz-Trejo, S. Quintero-Quintero, unpublished results.

[19] K. Oikawa, T. Kamiyama, S. Ikeda, T. Shishido, S. Yamaguchi, Solid State Ionics 154 (2002) 641–646.

[20] Hassan, S. Janes, R. Clasen, J. Eur. Ceram. Soc. 23 (2) (2003) 221–228.

[21] M. Yokosuka, Jpn. J. Appl. Phys. 32 (1993) 4578–4583.

[22] T. Takahashi, E.J. Wu, A. van der Ven, G. Ceder, Jpn. J. Appl. Phys. 39 (2000) 1241–1248.

[23] I. Sosnowska, R. Przenioslo, W. Kockelmann, R. Hempelmann, K. Wysocki, J. Alloy Compd. 328 (2001) 226–230.

[24] Y. Du, A.S. Nowick, J. Am. Ceram. Soc. 78 (11) (1995) 3033–3039.

[25] I. Sosnowska, W. Schäfer, R. Przenioslo, K. Lind, R. Hempelmann, Physica B 276–278 (2000) 864–865.

[26] E. Zimmer, K. Scharf, T. Mono, J. Friedrich, T. Schober, Solid State Ionics 97 (1–4) (1997) 505–509.

[27] M. Thirumal, A.K. Ganguli, Bull. Mater. Sci. 23 (6) (2000) 495–498.

[28] I. Levin, J.Y. Chan, R.G. Geyer, J.E. Maslar, T.A. Vanderah, J. Solid State Chem. 156 (2001) 122–134.

[29] J. Takahashi, T. Fujii, S. Shimada, K. Kodaira, J. Eur. Ceram. Soc. 19 (1999) 1089–1093.

[30] M. Fakhfakh, A. Kahn-Harari, A. Bulou, N. Jouini, J. Solid State Chem. 164 (2) (2002) 272–279;
M.J. Davis, M.D. Smith, H.C. zur Loye, Acta Crystallogr. C 57 (11) (2001) 1234–1236;
K.S. Chang, D.A. Keszler, Mater. Res. Bull. 33 (2) (1998) 299–304;
N. Floros, C. Michel, M. Hervieu, B. Raveau, J. Solid State Chem. 168 (1) (2002) 11–17;
Q.J. Yu, S. Sugita, X.J. Feng, J.X. Mi, Cem. Concr. Res. 27 (9) (1997) 1439–1449;
F. Goutenoire, V. Caignaert, M. Hervieu, C. Michel, B. Raveau, J. Solid State Chem. 115 (2) (1995) 508–513.

[31] J.T. Rijssenbeek, S. Malo, V. Caignaert, K.R. Poeppelmeier, J. Am. Chem. Soc 124 (10) (2002) 2090–2091.

[32] J.M. Jehng, I.E. Wachs, Chem. Mater. 3 (1991) 100–107.

[33] R.D. Shannon, Acta Crystallogr. A 32 (1976) 751–767.

[34] D. Stauffer, A. Aharony, Introduction to Percolation Theory, Taylor & Francis, London, 1992.

[35] H.G. Bohn, T. Schober, T. Mono, W. Schilling, Solid State Ionics 117 (1999) 219–228.

[36] I. Animitsa, A. Neiman, N. Kochetova, B. Melekh, A. Sharafutdinov, Solid State Ionics 162–163 (2003) 63–71.